ENGINEERING

An ultrathin rechargeable solid-state zinc ion fiber battery for electronic textiles

Xiao Xiao[1,2]†, Xiao Xiao[3]†, Yihao Zhou[1], Xun Zhao[1], Guorui Chen[1], Zixiao Liu[4], Zihan Wang[5], Chengyue Lu[5], Menglei Hu[6], Ardo Nashalian[1], Sophia Shen[1], Kedi Xie[3], Weiwei Yang[3], Yongji Gong[3]*, Wenbo Ding[5], Peyman Servati[6], Chao Han[2], Shi Xue Dou[2], Weijie Li[2]*, Jun Chen[1]*

Electronic textiles (e-textiles), having the capability of interacting with the human body and surroundings, are changing our everyday life in fundamental and meaningful ways. Yet, the expansion of the field of e-textiles is still limited by the lack of stable and biocompatible power sources with aesthetic designs. Here, we report a rechargeable solid-state Zn/MnO_2 fiber battery with stable cyclic performance exceeding 500 hours while maintaining 98.0% capacity after more than 1000 charging/recharging cycles. The mechanism of the high electrical and mechanical performance due to the graphene oxide–embedded polyvinyl alcohol hydrogel electrolytes was rationalized by Monte Carlo simulation and finite element analysis. With a collection of key features including thin, light weight, economic, and biocompatible as well as high energy density, the Zn/MnO_2 fiber battery could seamlessly be integrated into a multifunctional on-body e-textile, which provides a stable power unit for continuous and simultaneous heart rate, temperature, humidity, and altitude monitoring.

INTRODUCTION

Clothing is a critical factor of human society, as it reflects cultural identity and integrates cutting-edge technology. Leading the trend of next-generation point of care is the merging of electronics and textiles to develop a wireless textile body area network (TBAN) (*1*, *2*). The TBAN could continuously acquire physiological information and enable a change from the current reactive and disease-centric health care system to a personalized model that focuses on disease prevention and health promotion (*3*, *4*). As the society embraces the era of 5G and the internet of things (IoT), TBAN emerges as a compelling form of technology that can provide long-term, real-time, and precise point-of-care services ubiquitously while maintaining superior permeability, user comfortability, environmental stability, and mechanical robustness (*5*, *6*). Stability of the TBAN's power source to maintain its operation is critical; therefore, the TBAN needs a corresponding soft power source that will not compromise the integral conformability and wearability (*7*, *8*). Over the past decades, considerable efforts have been devoted to flexible supercapacitors and lithium-ion batteries for wearable bioelectronics (*9*–*11*). While flexible supercapacitors have high power density, their insufficient energy density and short discharge duration limit their practical applications (*12*, *13*). Flexible lithium-ion batteries have a higher energy density, but their intrinsic safety and potential environmental concerns restrict their widespread adoption in wearable electronics (*11*, *14*, *15*).

Because of its key characteristics such as high theoretical capacity, optimum safety, and low cost, zinc ion batteries (ZIBs) have gained an increasing attention for wearable electronics (*16*–*18*). Aqueous Zn/MnO_2 batteries with $ZnSO_4$/$MnSO_4$ electrolytes are considered one of the most promising candidates for flexible ZIBs due to their wide electrochemical windows, cost effectiveness, eco-friendliness, high specific capacity, and simple fabrication (*19*). Note that, when fabricating flexible ZIBs, conventional aqueous electrolytes are amorphous and cannot effectively segregate the electrodes to prevent short circuits under stretching or bending (*20*). As a result, gel electrolytes that consist of a polymer host and a corresponding aqueous electrolyte have been widely used in flexible ZIBs (*21*, *22*). According to Hofmeister's effect, SO_4^{2-} has a strong ability to precipitate commonly used polymer hosts; therefore, $ZnSO_4$/$MnSO_4$-based gel electrolytes are challenging to fabricate (*23*). Furthermore, the poor mechanical properties and low ion conductivity of present gel electrolytes also limit the application of flexible ZIBs in wearable devices (*24*). As a result, developing a high ion-conductive $ZnSO_4$/$MnSO_4$ gel electrolyte with compliant mechanical properties for flexible ZIBs is highly desirable and remains a challenge.

Here, we report a high-performance Zn/MnO_2 fiber battery using graphene oxide (GO)–embedded polyvinyl alcohol (PVA) hydrogel electrolytes (GPHEs) via the synergy of GO and $ZnSO_4$/$MnSO_4$ salting out. A low concentration of GO flakes is homogeneously distributed in the gel electrolyte as an "ion transport highway," where ion conductivity is created via a $ZnSO_4$/$MnSO_4$ solution soaking process. The ion transport properties of gel electrolytes were rationalized by Monte Carlo simulations and finite element analysis (FEA). The high ion conductivity (21 mS·cm^{-1}), favorable Young's modulus (530 kPa), high stretchability of ~230% strain without breakdown, and the self-healing capability of the gel electrolyte endowed the ZIB fiber with the capability of readily working under various conditions and maintaining 98.0% capacity during the charging-discharging for more than 1000 cycles. The rechargeable solid-state zinc ion fiber battery was demonstrated to stably drive a TBAN for continuous measurement of pulse, temperature, humidity, and pressure signals from volunteers. We envision that this work will provide a stable, cost-effective, and scalable approach that surpasses commercial flexible batteries and renders a sustainable and wearable power solution for electronic textiles (e-textiles).

[1]Department of Bioengineering, University of California, Los Angeles, Los Angeles, CA 90095, USA. [2]Institute for Superconducting and Electronic Materials, University of Wollongong, Wollongong, NSW 2522, Australia. [3]School of Materials Science and Engineering, Beihang University, Beijing 100191, China. [4]Department of Mechanical and Aerospace Engineering, University of California, Los Angeles, Los Angeles, CA 90095, USA. [5]Tsinghua-Berkeley Shenzhen Institute, Tsinghua University, Shenzhen 518055, China. [6]Department of Electrical and Computer Engineering, University of British Columbia, Vancouver, British Columbia V6T 1Z4, Canada.
*Corresponding author. Email: yongjigong@buaa.edu.cn (Y.G.); wl347@uowmail.edu.au (W.L.); jun.chen@ucla.edu (J.C.)
†These authors contributed equally to this work.

RESULTS

Fabrication of GPHE

As illustrated in Fig. 1A, there are three main steps in the preparation of GPHE: (i) mixing PVA and GO, (ii) freeze/thaw processing, and (iii) $ZnSO_4$/0.3$MnSO_4$ solution soaking (details in Materials and Methods). Theoretically, PVA with functional groups of hydroxyls is considered to be a candidate for constructing a gel electrolyte (*25*). However, the low elasticity, low ionic conductivity, and poor mechanical strength of PVA-based electrolytes constraint next-generation applications (*26*). To address this limitation, a reinforcement material with high interfacial attraction with PVA and effective ion transfer can be used. For example, GO flakes were exploited due to its ultrahigh specific surface area and abundant oxygen-containing functional groups (*27*, *28*). The insets of Fig. 1A show the three kinds of possible hydrogen bond structures contained in the PVA-GO complex. Using density functional theory (DFT) calculations, the average bond energy between PVA and GO was found to be −19.3 kcal/mol, which is comparatively greater than the value of intermolecular forces but less than the value of a covalent bond. Thus, this theoretically indicates that hydrogen bonds widely exist in our structure, which is confirmed by Raman spectrum and Fourier transform infrared tests (fig. S1). To interpret the dispersion effect of GO within a PVA hydrogel host on GPHE's ion conductivity, a schematic structure is proposed (Fig. 1B). The molecular chain of PVA acts as the framework for maintaining the stiffness, while the ions transport in the $ZnSO_4$/$MnSO_4$ solution

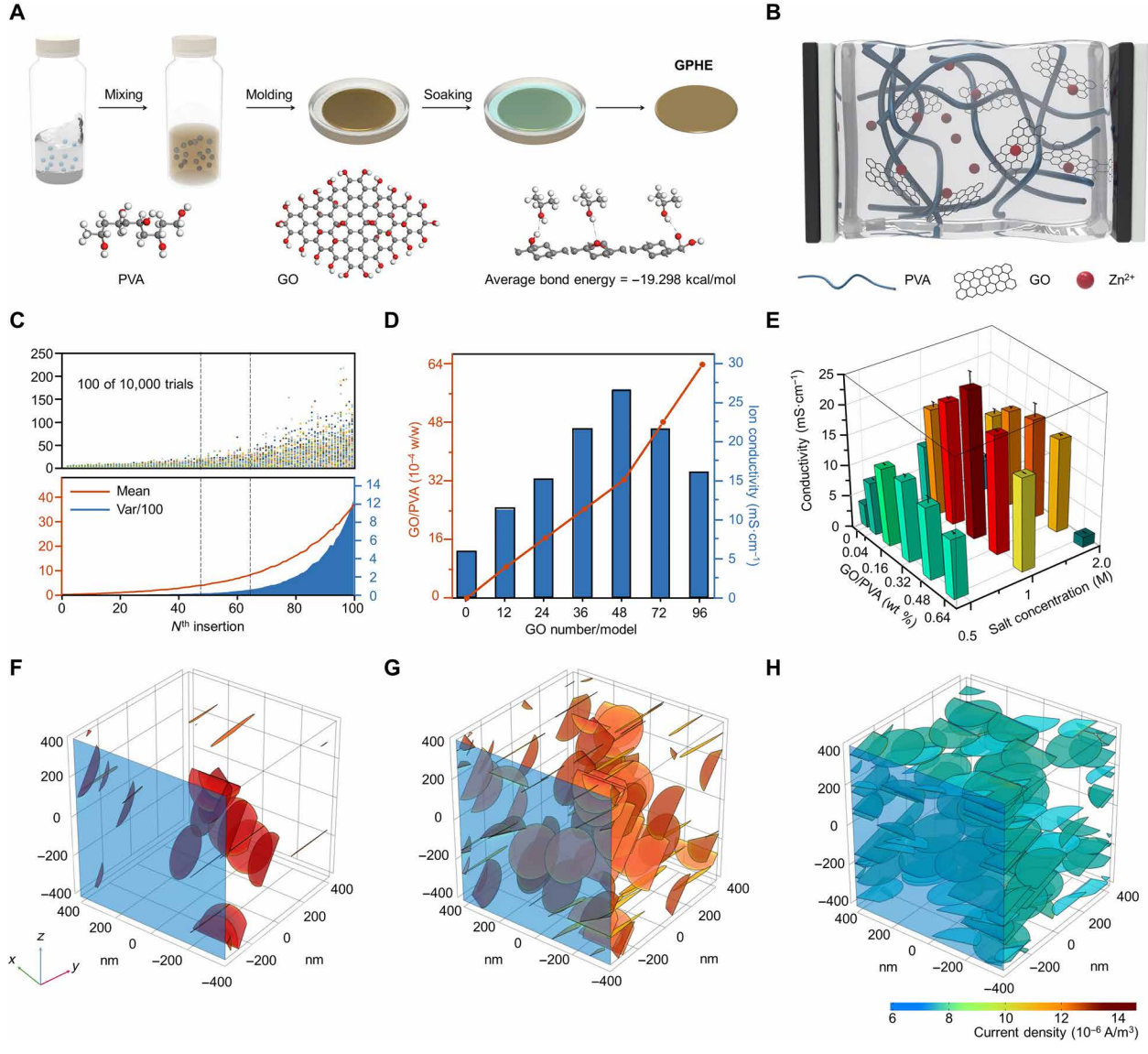

Fig. 1. Fabrication of GPHE. (**A**) Schematic diagram of the preparation process of GPHE. The inner image is the schematic diagram of three kinds of hydrogen bond formation between PVA and GO. (**B**) Schematic diagram of the ion-conducting process of GPHEs. (**C**) Monte Carlo simulation result of GO distribution state in PVA matrix. (**D**) Calculation results of ion conductivity of GPHEs with different GO mass. (**E**) Measurement ion conductivity of GPHEs with different PVA-GO mass ratios and soaking concentrations. (**F** to **H**) Maximum conductivity of models and calculation analysis of GPHEs, (F) with small GO mass, (G) with moderate GO mass, and (H) with excessive GO mass.

(fig. S2). The hydrogen bond formed between the GO and the PVA polymer influenced the dispersion of GO (*9*, *28*), which improved ion mobility and formed a layered structure that molecularly attached to the PVA polymer. Therefore, because of the homogeneous distribution of GO in a three-dimensional (3D) network formation in the GPHE, a high degree of continuous and interconnected ion transport pathways on the GO surface was formed, which can be viewed as a "highway" for ion transport.

The electrochemical performance of 2D material matrix composites has been a widespread concern. To explore how the concentration of GO in GPHE influences distribution states, we simulated the process of 100 GO flakes dispersed in GPHE (800 nm × 800 nm × 800 nm) 10,000 times using the Monte Carlo method. When there is an overlap between GO flakes, the overlapping GO flakes are removed and reinserted into the model, increasing the failure count by one each time. The experiment will continue until there is no overlap between any of the GO flakes. Figure 1C plots the failure numbers of the *n*th insertion in 100 of 10,000 simulations. Initially, the addition of the flake does not easily collide with previous ones, which indicates that the GO produces an independent positive contribution to the ion conductivity of GPHE. Although more flakes can be inserted into the matrix with more attempts, excessive GOs easily stack on top of each other. When the number of flakes is between 50 and 70, the number of failed attempts increases rapidly, and the system becomes unstable. Furthermore, when the number of flakes is larger than 70, the number of failed attempts increases more fiercely; these GOs tend to completely stack on top of one another, which is anticipated to deteriorate the ion conductivity. Such simulation methods can be further developed in other composite systems effectively, which brings a great potential for the development of related research fields.

On the basis of Monte Carlo simulation, a detailed FEA of the GO's random distribution in GPHE was applied by COMSOL Multiphysics (Fig. 1D and fig. S3). At a high molecular weight, the ion transport is ensured by microscopic processes independent of polymer length and thus of its viscosity (*29*). The main mechanisms proposed to describe the ion dynamics and their associated time scale are the following: (i) cooperative motion of ions and polymer segments, i.e., the ions use the chains as vehicles, (ii) motion of the ions along a chain, and (iii) jumps between different chains. On the basis of this, we assume an "ion highway" model for the simulation of GPHE conductivity, i.e., charge carriers can travel much faster on the GO nanosheet, thereby promoting the conductivity of the hydrogel at the macroscale. The charge carriers (Zn^{2+} and SO_4^{2-}) have different movement velocities on GO and PVA, which are proportional to the conductivity of pure GO material and PVA polymer substrate. Notably, the concentration of GO determines the concentration of nanosheet per unit volume and, to some extent, influences their direction preference, as depicted by the Monte Carlo simulation.

A series of GPHE with corresponding GO/PVA mass ratios soaking in different concentrations of $ZnSO_4$/0.3$MnSO_4$ solution was prepared. Their ion conductivities were determined on the basis of the impedance spectroscopy measurements, shown in Fig. 1E. The results are also verified by the COMSOL simulation by an integration of current density on all GO nanosheets. Therefore, as the current density of a single GO nanosheet declines as the GO concentration rises up, the density of GO nanosheets in the unite volume also increases, which predicts a turning point of ion conductivity at a proper GO concentration. As shown in Fig. 1F, 0.04 weight % (wt %) of GO makes a marked improvement of around 200% in ion conductivity. When the GO concentration reaches a weight ratio of 0.32 wt %, excessive GO nanosheets block the way of ion transportation and the elevation angle becomes smaller, leading to the stagnation of conductivity growth (Fig. 1G). Going beyond this certain range, the stacking effect intensified and led to a substantial decrease in elevation angle, which eventually offset the increase in conductivity (Fig. 1H). The perfect match of the simulation with the experimental results strongly supports our ion highway hypothesis model and offers an in-depth interpretation of the relationship between the dispersion and orientation of GO nanosheets and the concentration in the polymer system. This ionic highway can also maintain its capacity at higher temperatures, where activation energy for ion transport indicates that GO plays a positive role (fig. S4). On the basis of these results, the optimized GO/PVA ratio of 0.32 wt % was determined for the fabrication of GPHEs.

Performance of GPHE

Because of the weak conductivity of neutral gel electrolytes, the gel electrolytes that were previously reported are commonly alkaline, which suffer from notable degradation of coulombic efficiency and capacity during the cycling process (*30*). Moreover, organic salt-based electrolytes [e.g., Zn $(CF_3SO_3)_2$; table S1] are thousands of times more expensive than inorganic salts (e.g., $ZnSO_4$) and thus restrict them from widespread adoption. $ZnSO_4$/$MnSO_4$ solutions featuring wide electrochemical windows, high safety, and low cost are widely used as electrolytes for ZIBs. However, because of their strong tendency to precipitate in conventionally used polymers, $ZnSO_4$/$MnSO_4$-based gel electrolytes are challenging to fabricate (fig. S5). To address this issue, we propose to prepare Zn^{2+}/Mn^{2+}-doped hydrogel host by using a combination of freeze-thawing and soaking approaches (Fig. 2A). PVA-GO hydrogels were prepared via freeze-thawing treatments three times; subsequently, $ZnSO_4$/$MnSO_4$ was introduced into the PVA-GO hydrogel host via a solution-soaking treatment (Fig. 2B) (*31*).

However, ion conductivity is not always positively correlated to the concentration of soaking solutions. As the hydrogel shrinks due to high concentrations, the ion conductance will be reduced (fig. S6). Shrinkage of the hydrogel during salting out can also be simulated by chemical species transport and structural mechanics modules in COMSOL Multiphysics. After the GPHE was soaked in $ZnSO_4$/$MnSO_4$ solutions for 24 hours, its water content became ~40 and 60% of the original water content (table S2). The stress field is shown in Fig. 2C, where GPHE lost ~50% of its water content. Overall, an optimal high ion conductivity of 21 $mS{\cdot}cm^{-1}$ was achieved in the GPHE, where the soaking concentration of $ZnSO_4$/0.3$MnSO_4$ solution is 1 M and the mass fraction of GO/PVA is 0.32 wt %. Meanwhile, the concentration and closer packing of the polymer during freezing prepared the polymer chains for strong aggregation and crystallization induced by solution soaking (*32*, *33*). This process achieves a broad tunable range of mechanical properties that are closely related to the concentration of GO and soaking salt solution. Figure 2D shows the stress and strain measurement of the GPHE. In general, the GPHE gains a higher modulus and elongation capacity as the concentration of GO and salt solution rises, as a result of the strong hydrogen bond generated between the GO nanosheets and the PVA matrix (Fig. 2E and fig. S7).

Figure S8 demonstrates the melting curves of GPHE with different GO mass fractions. When the mass fraction of GO increases, the

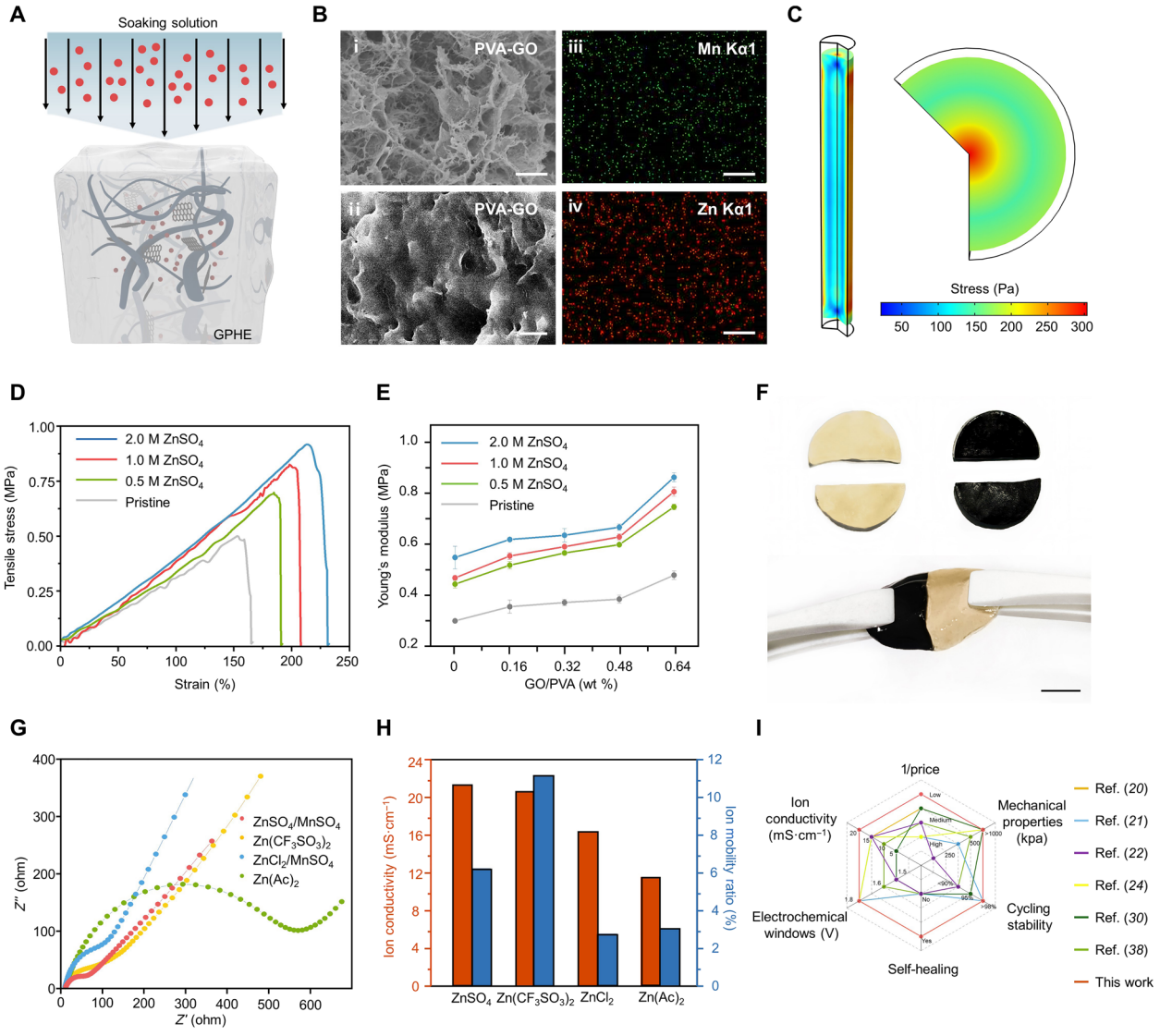

Fig. 2. Performance optimization of the GPHE. (**A**) Schematic of the soaking approach for salt ion penetration into the GPHEs. (**B**) Scanning electron microscopy (SEM) image of GPHE. Inset: (i) section view, (ii) front view, and (iii and iv) energy-dispersive spectrum. Scale bars, 5 μm. (**C**) Stress and deformation of GPHE after soaking in different $ZnSO_4$/0.3$MnSO_4$ solutions. (**D**) Tensile stress versus strain plots of the GPHE with different GO mass fractions under different $ZnSO_4$/0.3$MnSO_4$ as soaking salt solution. (**E**) Young's modulus of GPHEs with different components. (**F**) Self-healing capacity of GPHE; the black sample is dyed with black ink in hydrogel solution. Scale bar, 1 cm. Photo credit: Xiao Xiao, University of California, Los Angeles. (**G**) Impedance of GPHE soaking in different salt solutions, where $ZnSO_4$/$MnSO_4$ solution performed the minimum impedance under alternating current compared to other salt solution. (**H**) Ion conductivity and mobility of different salt-soaked GPHEs. (**I**) Comparison with previously reported electrochemical performances of gel electrolytes and other solid-state electrolytes (see table S3 for details).

melting peaks of GPHE shift slightly to the lower temperature, indicating that the addition of GO decreases the degree of crystalline. The phase structure was also examined using x-ray diffraction (XRD) and small-angle x-ray scattering characterization (figs. S9 and S10). The GO tends to interact with the PVA to form an amorphous phase on the GO surface and decrease the overall crystalline degree of GPHE. The $ZnSO_4$/$MnSO_4$ ions can easily migrate through the disordered amorphous phase (transport pathway). In addition, to demonstrate the self-healing ability of the GPHE, two pieces of GPHE, one of which was colored by black ink, were cut in the middle, respectively (step I of Fig. 2F). Under external force, the PVA chain segments would break, and a large number of free-moving PVA chain segments without physical crystallization would expose on the fresh fracture surface. Once the two pieces of hydrogels were brought into contact, these free-moving PVA chain segments would attract each other by hydrogen bonds. With the increase of contact time, more uncrystallized PVA chain segments could move toward the fracture surface to reestablish more hydrogen bonds and finally realize complete self-healing (step II of Fig. 2F and movie S1).

The ionic conductivity and ion mobility ratio of GPHE were determined from the AC impedance spectra (Fig. 2G). The high ion conductivity is attributed to the enhanced dissociation of the $ZnSO_4$/$MnSO_4$ solution, where GO acts as the additional dielectric substance and facilitates ion transport in the GPHE. Therefore, this

highway built by a 3D network of GO results in higher ion conductivity. Moreover, compared with other salt solutions mentioned in previous works, such as $Zn(CF_3SO_3)_2$ and $ZnCl_2$, GPHE treated by $ZnSO_4/0.3MnSO_4$ salt solution has a higher ion conductivity, of around 20 mS·cm^{-1} (Fig. 2H). Notably, the overall performance of GPHE is also one of the best among representative research on zinc ion gel electrolytes over the past 3 years (Fig. 2I and table S3) (*7*, *21*–*23*, *25*, *31*, *34*, *35*).

Rechargeable solid-state ZIB

Because the fabrication of GPHE involves a process of converting the liquid into a hydrogel state, the cathode and anode could be integrated into one monolith with continuous and seamless interfacial connection through the gel electrolyte. Compared to conventional stacked architectures, all-in-one structures could ensure continuous and effective loading and ion transfer capacity under external deformation. This is because the monolith architecture avoids the relative displacement or detachment between the neighboring component layers, resulting in excellent structural and electrochemical stability. Furthermore, all-in-one integrated configurations could also effectively reduce the thickness of devices by simplifying the structure, which is beneficial to enhancing their flexibility and electrochemical performance. In our case, a nano-MnO_2 cathode was prepared by the hydrothermal method, whose process is shown in Materials and Methods (Fig. 3A) (*36*, *37*). From XRD, x-ray photoemission spectroscopy (XPS) characterization, and scanning electron microscopy (SEM) images, the as-prepared nano-MnO_2 shows high crystallinity and clear layered nanostructure. Compared to commercial pristine MnO_2, nano-MnO_2 is thinner and shorter, and its crystal lattice appears to be imperfect due to the oxygen-deficient fragmented layers (figs. S11 to S13). The

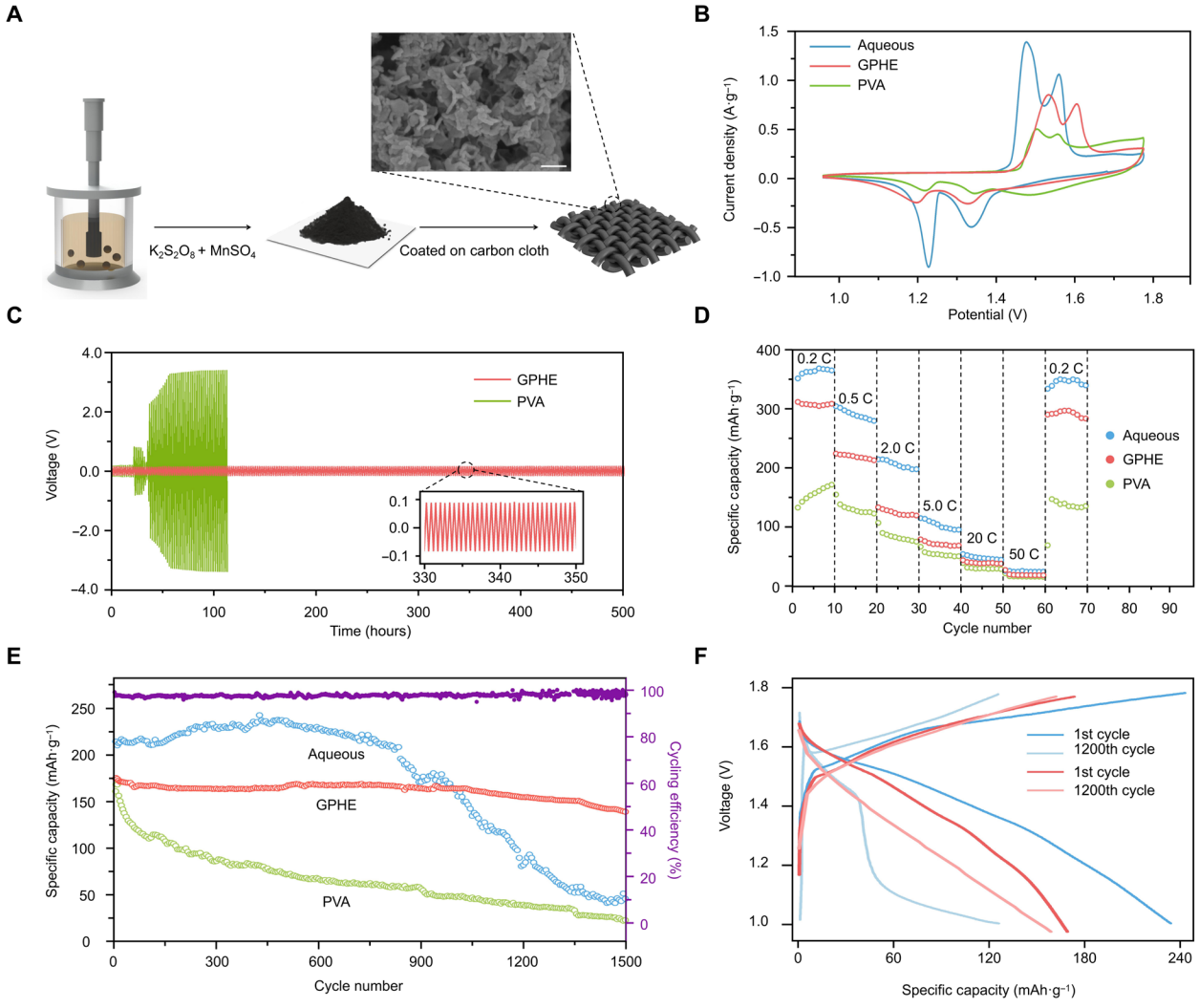

Fig. 3. Electrochemical performance of the rechargeable solid-state ZIB. (**A**) Preparation process of nano-MnO_2 cathodes on carbon cloths. Inset: SEM image of the nano-MnO_2 coated on carbon film. Scale bar, 500 nm. (**B**) Cyclic voltammetry (CV) curves at a scan rate of 0.05 mV·s^{-1}. (**C**) Galvanostatic charge and discharge (GCD) profiles of ZIB with GPHE, PVA, and aqueous electrolytes at 2 mA·g^{-1}. Inset: Enlarged view of GCD profile of GPHE cell. (**D**) Rate performance of Zn/MnO_2 batteries with aqueous electrolyte, PVA electrolyte, and GPHE Coin cells, in which the GPHE performed best stability in all cycling rates. (**E**) Cycling performance of coin cells with aqueous electrolyte, PVA electrolyte, and GPHE at a current density of 0.3 A·g^{-1}. (**F**) Comparison of voltage capacity profile of coin cells between first cycle and 1200 cycles of aqueous electrolyte (blue) and GPHE (red).

defects of nano-MnO_2 cathode reduced the Gibbs free energy of Zn^{2+} adsorption, leading to a more readily efficient ion transference process that reduces interface resistance.

The electrochemical performance of GPHE in Zn/MnO_2 fiber batteries was first investigated in coin cells. At a scan rate of 0.05 $mV{\cdot}s^{-1}$, the cyclic voltammetry (CV) curves display two pairs of reduction/oxidation peaks at 1.50/1.65 and 1.24/1.38 V (Fig. 3B). They can be ascribed to a two-step redox reaction associated with Zn^{2+} ion insertion/extraction of the layered nano-MnO_2 cathode, corresponding to the changes of manganese from Mn^{4+} to Mn^{3+} and Mn^{3+} to Mn^{2+}, respectively. Such results agree well with the galvanostatic charge/discharge (GCD) profiles, where the voltage plateaus are observed at a similar potential (Fig. 3C). The voltage-time curve shows that the GPHE-based cell was stabilized around 90 mV for more than 500 hours, whereas other cells based on PVA-gel electrolytes exhibited large increases in voltage hysteresis, particularly after 120 hours. Also, the GPHE ensures fast Zn^{2+} ion diffusion, enabling the high-rate capability and outstanding cycling stability. The capacity of Zn/MnO_2 batteries with aqueous electrolyte, PVA-gel electrolyte, and GPHE was compared under different cycling rates (Fig. 3D). Moreover, even after 1000 cycles at a high current density of 0.3 $A{\cdot}g^{-1}$, the capacity of the integrated fabrication remained 98.0% and was 75.4% after 1500 cycles (Fig. 3E). Compared to the substantial degradation of coin cells with aqueous electrolyte and PVA-gel electrolyte, the all-in-one GPHE ZIB demonstrated its remarkable superiority (Fig. 3F). Such stable cycle performance can be credited to the outstanding ion conductivity, electrochemical stability of GPHE, and excellent interface stability among different components posed by the all-in-one structure.

Integrate fiber battery into clothing

Fusing biomedical electronics with textiles is becoming a popular trend nowadays (*38*–*41*). Traditional batteries with a rigid structure, limited lifetime, and heavy weight are not an ideal power source for e-textiles, whereas the ZIB fiber offers a superior substitute. This work aims to develop a flexible, sustainable, and stable energy storage solution to drive the TBAN for continuous point of care. As schematically illustrated in Fig. 4A, the flexible ZIB energy hub takes ZIB fibers as building blocks. Starting with zinc wires and nano-MnO_2–coated carbon wires, a MnO_2 electrode and a zinc electrode were buried inside the GPHE. Then, an ultrathin (diameter of 1 mm), lightweight (weight of 1.26 g per 15 cm), low-cost ($0.64 per 15 cm), high-volume energy density (91 $Wh{\cdot}L^{-1}$), and rechargeable Zn/MnO_2 fiber battery (for calculation detail, see Supplementary Text) was assembled by the self-healing process and encapsulated in a layer of silicone to avoid potential contact of the electrolyte with human skin (Fig. 4B). The self-healing features of the ZIB fibers can prevent it from open circuit or short circuit.

In addition, one key challenge in daily wear is building a highly safe and flexible energy storage device that can be bent, punctured, and even soaked in water while maintaining their electrochemical functions under mechanical deformations. As presented in Fig. 4C, the ZIB fiber is highly flexible to fit human skin and also exhibits excellent mechanical robustness. The capability of the ZIB fiber under bending is demonstrated in Fig. 4D. Its form remained consistent when bent to various angles or completely folded. The bending stress and deformation of a 3-cm-long ZIB fiber subjected to 2 N vertical loads at the two ends were acquired by COMSOL Multiphysics, as shown in the inner image. This magnitude of load can be easily provided by human muscles without any burden or injury. Zinc and carbon wires have good strain compatibility with GPHE and silicone. During large deformation, the composited structure is tightly assembled without any decohesion and separation, which ensures the reliability and safety in use. The Young's modulus of the ZIB fiber is comparable or less than that of human soft tissues and materials, such as elastin (~0.6 MPa), resilin (~1.8 MPa, dry state), arteries (~0.3 MPa), and skin (~0.42 MPa for the young and ~0.85 MPa for the older). Therefore, the ZIB fiber can deform well with biological tissues and has a good biocompatibility. Moreover, attributed to the encapsulation process, the ZIB fiber is stable in the air and waterproof, enabling it to continuously produce electricity in daily living conditions (Fig. 4E). The experimental results show that the stored energy in the fiber can carry out stable release and recharge under water conditions without notable capacity loss after more than 500 electrochemical cycles (Fig. 4F). After more than 500 cycles of continuous twisting, its capacity remains almost the same as its original value (Fig. 4G). Overall, the flexible ZIB energy hub demonstrated superior energy and power density compared to existing works. Together with its compelling features such as light weight, flexibility, and weavability, the flexible ZIB energy hub serves as a suitable candidate for unprecedented wearable power supply (Fig. 4H).

Stable power source for TBAN

Inspired by this notion, we here propose and demonstrate the concept of a TBAN: A modularized, textile-based system with various functions powered by flexible ZIB fibers (Fig. 5A). The TBAN concept was realized with multiple sets of sensors and circuits embedded in clothes. The network contains one smartphone with four sensor nodes, where the number and types of sensors or actuators can be readily modified according to personalized demand (*42*–*44*). As a proof of concept, the network consists of a photoplethysmography (PPG) sensor, a temperature sensor, a humidity sensor, and a barometer. The PPG sensor was designed at the cuff for heart rate detection, while other sensors were located at the upper front body for environmental monitoring. The signals from each sensor were first acquired by the microcontroller unit (MCU), which subsequently sent all collected data to the smartphone via a Bluetooth low-energy (BLE) protocol (fig. S14). Through the graphical user interface on the smartphone, all the collected pulse, respiration, and body movement data can be simultaneously displayed. As shown in Fig. 5B, the ZIB fibers are used to drive the TBAN. In addition, the ZIB fiber charges bidirectionally with smart devices that support wireless charging, such as a smart phone, smart watch, or smart headset (Fig. 5C). Also, a screen was deployed to indicate the battery level. Furthermore, the ZIB fiber was waterproof to meet the need for washing clothes in real life (Fig. 5D and movie S2) (*34*, *35*). All electronic components and sensors (represented by MCU) were treated with waterproof coating: light and transparent polydimethylsiloxane polymer, as shown in fig. S15.

Previous studies only demonstrated a proof-of-concept design in in vitro settings and were rarely deployed in practical wearing conditions. In the first demonstration, we tested the performance of the as-constructed system in an outdoor environment. Filmed at a hilly terrain, one of the coauthors climbed the hill wearing the TBAN (Fig. 5E). The TBAN system monitors the wearer's heart rate and environmental conditions, such as temperature, humidity, and altitude, in real time, which indicates a confirmation for stable performance of the TBAN, even when the wearers are performing

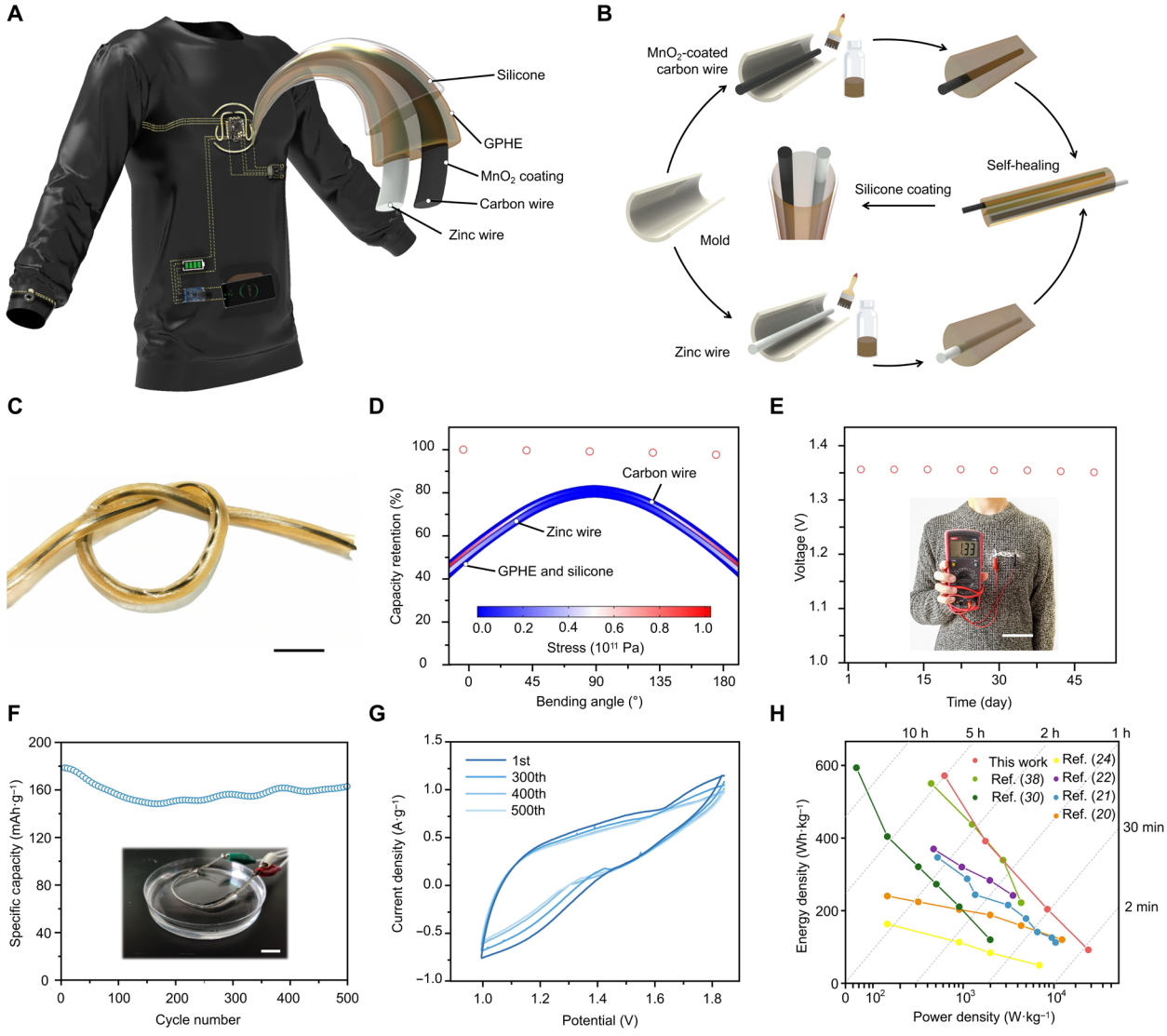

Fig. 4. Integrating solid-state ZIB fiber into clothing. (**A**) Illustration and design of a flexible ZIB TBAN. (**B**) Fabrication process of the functional fibers as the building blocks. (**C**) Photograph of GPHE-based ZIB fiber, illustrating its excellent flexibility. Scale bar, 2 mm. Photo credit: Xiao Xiao, University of California, Los Angeles .(**D**) GPHE-based ZIB fiber maintaining stable capacity output under different bending angles. Inset image shows bending stress and deformation of a 3-cm ZIB fiber. (**E**) GPHE-based ZIB fiber maintaining stable voltage output in long-term standing. Scale bar, 10 cm. Photo credit: Xiao Xiao, Beihang University. (**F**) Cycling stability of GPHE-based ZIB fiber at a current density of 0.3 $A{\cdot}g^{-1}$. Scale bar, 1 cm. Photo credit: Xiao Xiao, Beihang University. (**G**) CV curves of GPHE-based ZIB fiber at a scan rate of 0.05 $mV{\cdot}s^{-1}$. (**H**) Ragone plot of GPHE-based ZIB fiber in comparison to the existing works, indicating relationship between energy density and power density.

strenuous exercise in an outdoor environment (movie S3). In the second demonstration, the ZIB fibers are integrated into a knitted shirt with wearable sensors and a wireless charging terminal, which was built into a TBAN for sensor power supply and wireless charging (Fig. 5F). To further illustrate the convenience and sensitivity of the TBAN, we filmed some video clips to show the capability of a TBAN to charge wirelessly, transmit data wirelessly, and produce a graphical display on the smartphone. These two examples show the capability of the TBAN to perform multiple-dimension, long-term, continuous, and hands-free monitoring. Compared to traditional rigid battery-powered designs, our design improves the robustness and wearing comfort of the TBAN, envisioning an all-in-cloth wearable electronics system.

DISCUSSION

In this work, GPHEs were successfully fabricated on the basis of two common materials—GO flakes and a PVA hydrogel matrix, where ion conductivity was achieved via a $ZnSO_4/MnSO_4$ solution soaking process. It exhibits high ion conductivity (21 $mS{\cdot}cm^{-1}$), low Young's modulus (530 kPa), high stretchability (up to 230% strain without failure), and self-healing ability. The high ion conductivity was verified and explained via Monte Carlo simulations and FEA. Also, a rechargeable solid-state zinc ion fiber battery was developed, demonstrating a collection of compelling features such as ultra-thinness (diameter of 1 mm), light weight (weight of 1.26 g per 15 cm), low cost ($0.64 per 15 cm), high-volume energy density (91 $Wh{\cdot}L^{-1}$), stable cyclic performance exceeding 500 hours, and maintenance of.

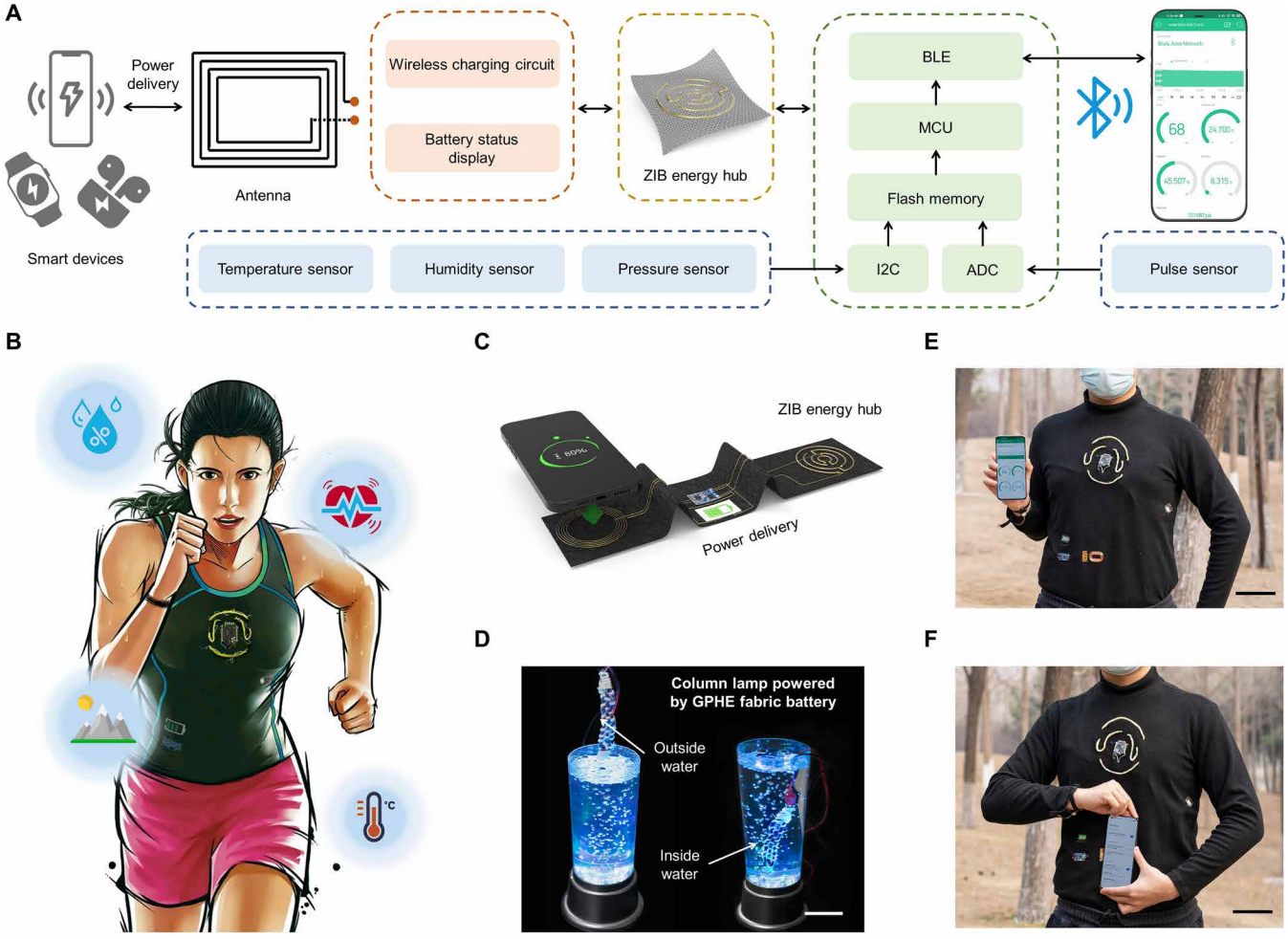

Fig. 5. Powering a TBAN. (**A**) Block diagram of the wearable system of the flexible ZIB-powered TBAN. (**B**) Illustration of wireless TBAN powered by ZIB fibers consisting of interconnected wearable sensors on clothing. The data collected by TBAN are uploaded to the cloud by Bluetooth for real-time body-state monitoring and telemedicine care. (**C**) Textile-based wireless power delivery between the smart phone and ZIB fibers. Photo credit: Xiao Xiao, University of California, Los Angeles. (**D**) GPHE fabric ZIB maintaining stable voltage output underwater. Scale bar, 10 cm. Photo credit: Xiao Xiao, University of California, Los Angeles. (**E**) Photograph of the application of body-state monitoring, with a coauthor wearing the TBAN in the outdoor environment. Scale bar, 10 cm. Photo credit: Xiao Xiao, Beihang University. (**F**) Photograph of convenience wireless charging of the TBAN. Scale bar, 10 cm. Photo credit: Xiao Xiao, Beihang University.

98.0% capacity after more than 1000 charging-recharging cycles. Toward practical applications, the solid-state Zn/MnO_2 fiber battery was demonstrated to power a TBAN for continuous monitoring of various physiological signals and wireless charging. The lightweight, low-cost, and high-performance Zn/MnO_2 fiber battery can be mass produced, showing an untapped potential of powering e-textiles for personalized health care.

Approaching the era of IoT, on-body electronics have been ushered in revolutionary changes and rapid growths. The demand for multifunctional material innovation, long-term durability, and biocompatibility of wearable electronics is becoming a hot topic. This work demonstrated a modularized, textile-based system powered by flexible ZIB fibers as a pioneering road map toward a mature system with output stability, long-lifespan safety, scalable design, and wearing comfort. However, challenges still remain in both energy storage and functional components. Despite the admirable efforts for the development of ZIB in the last decade, the three main intrinsic problems of ZIB systems are still hindering further development: (i) the low specific capacity compared with commercial Li-ion batteries, (ii) the retention of the electrode structure in the long cycling life, and (iii) the stable industrial process to ensure the quality of large-scale production. Meanwhile, the development of functional devices is limited in ultrathin miniaturization, heterogeneous integration, and flexibility. Fortunately, recent findings suggest promising next-generation solutions by evolving engineering constraints. Consequently, a brand-new smart cloth system would come into being for a future of much more convenience, comfort, and safety.

MATERIALS AND METHODS

Materials for GPHE and ZIB fiber

The following materials were used: PVA [weight-average molecular weight (M_w) of 146,000 to 186,000 and degree of hydrolysis of 98.0

to 98.8%; Acros], zinc sulfate heptahydrate (99.5%; Innochem), manganese(II) sulfate monohydrate (99.99%; Innochem), potassium thiosulfate (95%; Sigma-Aldrich), GO dispersion (0.5 mg/ml; one to five layers; XFNano), zinc foil (99.99% metals basis; Innochem), silicone [polydimethylsiloxane (silicone) emulsion; Alfa Aesar], zinc wire (99.99%), conductive carbon cloth and wire (TORAY T-300), and polyimide film (0.008 mm; Alfa Aesar).

Fabrication of GPHE

GPHE was fabricated following a three-step procedure: (i) preparation of 0.32 wt % PVA-GO viscous flow gel substrate, (ii) freeze-and-thawing process for gel crosslinking, and (iii) solution adsorption method for zinc ion penetration in gel electrolyte. For step (i), 4.25 g of PVA powder was dissolved in 50 ml of deionized water at 90°C under magnetic stirring for 1 hour to form a uniform solution. When microcrystalline particles could not be observed, GO solution was gradually added drop by drop into the as-prepared PVA solution under magnetic stirring for another 1 hour. Afterward, the uniform PVA-GO solution was cast onto a clean 3D printed photosensitive resin mold for crosslinking treatment. For step (ii), the mold containing PVA-GO solution was refrigerated at −6°C for 18 hours and was melted at room temperature for 6 hours to form dense crosslinking knots inside the gel base. The freeze-and-thawing process was repeated three times to transform the quasi-solution state gel into the solid-state gel. Last, for step (iii), the solid-state PVA-GO gel was soaked into the $ZnSO_4/MnSO_4$ solution (prepared by dissolving salt powder into deionized water) of different concentrations for 1 day to prepare GPHEs. In this process, the ions in the salt solution will penetrate into the PVA-GO gel so that the mechanical strength and conductivity of the gel could be greatly reinforced.

Synthesis of cathodes

The aqueous-based reaction solution was prepared by mixing 0.755 g of $MnSO_4$ and 1.35 g of $K_2S_2O_8$ into 100 ml of deionized water. Afterward, 25 ml of 1.2 M NaOH solution was added by droplets into the mixed solution at room temperature under magnetic stirring for 1 hour, followed by another hour of aging process. After the aging process, the supernatant of the solution was poured out and filtered with deionized water and ethanol to wash out the residual NaOH in the as-prepared nano-MnO_2 powders. Then, the nano-MnO_2 powders underwent freezing and drying for 2 days and then mixed with polyvinylidene difluoride, Carbon Nanotube, and Super-p at a ratio of 7:1:1:1 in a 5-ml beaker. Twenty-five droplets of *N*-methyl-2-pyrrolidone solution were added to the beaker and stirred for 3 hours to synthesize the cathode material. Last, the as-prepared slurry was coated on the carbon cloth and dried at 85°C for 12 hours to form the nano-MnO_2 cathode.

Preparation of flexible ZIB fiber

The intrinsic self-healing characteristic of GPHE plays a vital role in combining GPHE and electrodes to produce a flexible ZIB fiber with miniaturized diameter and maximum length. To examine the self-healing property in battery fabrication, thin-film electrodes are adopted. The as-prepared nano-MnO_2 foam or Zn foam was placed into the predesigned 3D printing resin mold in advance. Then, liquid-state PVA-GO gel solution was injected until the thin-film electrode placed at the bottom was completely coated in the gel solution. After freezing at −6°C for 1 hour and thawing at room temperature, the shape of gel electrolyte stabilized from the viscous phase. Then, another piece of electrode was also placed in the mold and coated with viscous gel solution and going through the same freeze-and-thawing process. Afterward, the two electrodes with solidified gel electrolyte were kept in close contact by the gel electrolyte interface. Because of the hydrogen bonding effect, the healing area propagates from the original point until the hydrogen bonding is formed in the whole crack area. After 10 min at room temperature, the crack healed completely, and the thin-film electrodes became the cathode and anode of an all-in-one flexible battery. The all-in-one flexible ZIB was frozen again at −6°C to start the freezing-thawing process and then underwent the solution adsorption process and silicone coating.

On the basis of the above procedure, the preparation of fiber cells is a method of forming separately and assembling by self-healing property of GPHE (Fig. 4B). Bare zinc wire anode and nano-MnO_2–coated carbon wire (fig. S16) were fixed separately in the 3D printed resin molds. After that, liquid-state PVA-GO gel was injected until electrode wire was fully immersed. Similar to the methods mentioned earlier, the surfaces of the half-cylinder gel electrolytes are kept face to face in close contact to prepare an all-in-one ZIB fiber. Afterward, the as-prepared fiber batteries are absorbed into the salt solution. Last, the as-prepared battery fabric was encapsulated with a spin-coating machine to form a thin layer of silicone for waterproof treatment.

Circuitry design of TBAN

The core circuitry of the TBAN was composed of a wearable printed circuit board (PCB) integrated with an ATmega328 microprocessor for signal processing and a Texas Instruments CC2540 Bluetooth low-energy module for wireless communication. Peripheral sensors connected to the MCU via input/output ports enabled various smart applications. The SON1303 PPG sensor, connected to the analog port, provided a low-cost and noninvasive heart rate estimation. The BOSCH BME280 Micro-electromechanical Systems (MEMS) environment sensor was connected to the MCU via Inter-Integrated Circuit (I2C) protocol, which monitored the temperature, humidity, and air pressure with high accuracy and ultrasmall form factor. All the sensor readings were sent to the smartphone via Bluetooth Low Energy (BLE) function and then uploaded to the cloud server. The power supply and power management circuit were also crucial to the circuitry. The wireless charging circuit complies with mainstream Wireless Power Consortium (WPC) Qi protocol, which provides a maximum 5 W of charging power and can automatically stop charging once the foreign objects are detected between the charging coil and smart devices. The TP4056 battery management chip was selected to monitor the battery temperature and prevent overcharging or overdischarging and was connected with a light-emitting diode (LED) display to indicate battery remaining capacity.

DFT simulation of the hydrogen bond structure between GO and PVA

We performed energy calculation by Gaussian with B3LYP basis set for geometry optimization of GO and PVA. Then, we performed energy calculation for GO, PVA, and PVA-GO complex by MP2/631-G(d) basis set, while for the complex, we added basis set superposition error (BSSE) correction.

Monte Carlo simulation of GO distribution state in PVA matrix

The 3D Monte Carlo simulation was deployed in Python environment. Because the thickness-to-diameter ratio of GOs is negligible,

it could be easily considered as a flake. For each epoch, the circular flake in the PVA matrix was first generated randomly and uniformly. Then, the distance $m_{i,j}$ between every two flakes was calculated (*45*). If the distances between a newly generated disk and previous ones were less than the minimum threshold, the attempt was rejected and recorded. Then, the insertion was reattempted until the number of flakes achieved the preset upper bound. We repeated this simulation 10,000 times to obtain the convergent data. All the simulation steps are presented in Algorithm 1.

Algorithm 1: Monte Carlo simulation of GO distribution states in PVA matrix

```
Setting up the parameters of simulation
for each epoch do
reset flake list D
reset attempt number(s) list A
while length of flakes list <100 do
generate a flake d_n
reset intersect I to False
for d in D do
compute the minimum distance m between d_n and d
if m < M than
a = a + 1
set I to True
break
if I is False then
add d_n to D
add a to A
a = 0
save D, A
```

Basic parameters:
1) Minimum distance M = 4 nm
2) Length of matrix side = 800 nm
3) The radius of flakes = 120 nm
4) The maximum number of flakes in matrix n_{max} = 100

FEA simulation of GPHE conductivity with different GO mass fractions

Finite element simulation was carried out on the COMSOL Multiphysics. The system mainly consisted of GO nanosheets of different angles to the current direction (set as z axis) and the PVA polymer matrix. During the charging process, the current density distribution on the upper and lower surfaces of the model under DC voltage was simulated, and the corresponding current value was obtained through integral operation to calculate the overall conductivity. Moreover, the angle of GO nanosheets in the system was simplified as a variation of elevation coefficient n and distribution number N:

1) Take three base elevation angles (based on XY plane): 10° [x axis (1,0,0)], 8° [Y axis (0,1,0)], and 15° [45° axis (1,1,0)].

2) The direction of GO nanosheets is decided by elevation coefficient n and base elevations as $n \times 10°$ [x axis (1,0,0)], $n \times 8°$ [Y axis (0,1,0)], and $n \times 15°$ [45° axis (1,1,0)] in XY plane.

3) GO nanosheets are randomly distributed in the periodic square (take the edge length: 800 nm), and the amount of GO nanosheets at each elevation is equal (distribution number is N).

Basic parameters:
1) Conductivity of ions on PVA base: 9.75 mS·cm^{-1} (experimentally measured)
2) Conductivity of ions on GO nanosheet: 4.65 S·m^{-1} ($ZnSO_4$/0.3$MnSO_4$ solution)
3) GO nanosheet radius: r_{GO} = 121.1 nm (XFNano)
4) GO nanosheet thickness: $L_{GO} = r_{GO}/100$
5) GO density: ρ_{GO} = 0.79 g·cm^{-3}
6) PVA density: ρ_{PVA} = 1.275 g·cm^{-3}

FEA simulations of GPHE shrinkage during soaking process

To simulate the deformation and stress of the ZIB fiber, the chemical species transport and structural mechanics modules of COMSOL Multiphysics are applied. Both the polymer chains and water are assumed incompressible; thus, the volumetric change of GPHEs is completely due to the transport of water molecules. The ratio between current and initial (unshrink) volume is given by

$$J = \frac{dV}{dV_0} = \det(\mathbf{F}) = \frac{\Omega C + 1}{\Omega C_0 + 1}$$

where $\mathbf{F}$ is the deformation gradient of gel structures; C and C_0 are current and initial water concentrations (defined as the number of water molecules per unit volume) in hydrogels, respectively; and Ω is the volume of a water molecule. The degree of shrinkage in all three dimensions of GPHEs should be the same due to isotropy. The stretch defined as the ratio between the current length and initial length can be calculated by $\lambda = J^{1/3}$.

The transport of water molecules driven by a gradient of chemical potential is governed by

$$\frac{\partial C}{\partial t} = \nabla \cdot (\mathbf{D} \cdot \nabla \mu)$$

where $\mathbf{D}$ is the diffusivity tensor of water molecules in the GPHE and μ is the chemical potential, related to $\partial W/\partial C$. The free energy W ($\mathbf{F}$, C) of a hydrogel consists of an elastic energy part W_{el} ($\mathbf{F}$) of polymer chains as a function of deformation gradient $\mathbf{F}$ and a mixing energy part W_{mix} (C) that is related to concentration C. The detailed analytical expression for W ($\mathbf{F}$, C) can refer to literature (*46*) The time-dependent concentration $C(t)$ of water molecules can also be obtained through the melt curves in fig. S8.

Mechanical characterization of ZIB fiber by FEA

To simulate the deformation and stress of the ZIB fiber, the solid mechanics module of COMSOL Multiphysics is applied. The length of the fiber used in Fig. 4D is 3 cm. The middle point of the fiber is fixed, and the two ends are subjected to concentrated vertical loads. The magnitude of the concentrated vertical load is 2 N. The driven forces are assumed to mimic human muscles. The constitutive laws for all component materials of the ZIB fiber can be considered as linear elastic. Note that the stress-strain relationships of GPHEs with different GO mass fractions under $ZnSO_4$ as soaking salt solution are shown in Fig. 2D. Before structural failure, the stress-strain relationship is approximately linear. The other important geometrical and mechanical parameters are listed in table S4.

SUPPLEMENTARY MATERIALS

Supplementary material for this article is available at https://science.org/doi/10.1126/sciadv.abl3742

REFERENCES AND NOTES

1. B. Chu, W. Burnett, J. W. Chung, Z. Bao, Bring on the BodyNET. *Nature* **549**, 328–330 (2017).
2. Y. Fang, G. Chen, M. Bick, J. Chen, Smart textiles for personalized thermoregulation. *Chem. Soc. Rev.* **50**, 9357–9374 (2021).
3. X. Tian, P. M. Lee, Y. J. Tan, T. L. Y. Wu, H. Yao, M. Zhang, Z. Li, K. A. Ng, B. C. K. Tee, J. S. Ho, Wireless body sensor networks based on metamaterial textiles. *Nat. Electron.* **2**, 243–251 (2019).
4. R. Lin, H. J. Kim, S. Achavananthadith, S. A. Kurt, S. C. C. Tan, H. Yao, B. C. K. Tee, J. K. W. Lee, J. S. Ho, Wireless battery-free body sensor networks using near-field-enabled clothing. *Nat. Commun.* **11**, 444 (2020).
5. G. Chen, Y. Li, M. Bick, J. Chen, Smart textiles for electricity generation. *Chem. Rev.* **120**, 3668–3720 (2020).
6. X. Shi, Y. Zuo, P. Zhai, J. Shen, Y. Yang, Z. Gao, M. Liao, J. Wu, J. Wang, X. Xu, Q. Tong, B. Zhang, B. Wang, X. Sun, L. Zhang, Q. Pei, D. Jin, P. Chen, H. Peng, Large-area display textiles integrated with functional systems. *Nature* **591**, 240–245 (2021).
7. N. Zhang, F. Huang, S. Zhao, X. Lv, Y. Zhou, S. Xiang, S. Xu, Y. Li, G. Chen, C. Tao, Y. Nie, J. Chen, X. Fan, Photo-rechargeable fabrics as sustainable and robust power sources for wearable bioelectronics. *Matter* **2**, 1260–1269 (2020).
8. Y. Zhou, X. Zhao, J. Xu, Y. Fang, G. Chen, Y. Song, S. Li, J. Chen, Giant magnetoelastic effect in soft systems for bioelectronics. *Nat. Mater.* **20**, (2021); https://doi.org/10.1038/s41563-021-01093-1.
9. X. Yang, F. Zhang, L. Zhang, T. Zhang, Y. Huang, Y. Chen, A high-performance graphene oxide-doped ion gel as gel polymer electrolyte for all-solid-state supercapacitor applications. *Adv. Funct. Mater.* **23**, 3353–3360 (2013).
10. X. Chu, G. Chen, X. Xiao, Z. Wang, T. Yang, Z. Xu, H. Huang, Y. Wang, C. Yan, N. Chen, H. Zhang, W. Yang, J. Chen, Air-stable conductive polymer ink for printed wearable micro-supercapacitors. *Small* **17**, 2100956 (2021).
11. R. F. Service, Zinc aims to beat lithium batteries at storing energy. *Science* **372**, 890–891 (2021).
12. H. Li, C. Han, Y. Huang, Y. Huang, M. Zhu, Z. Pei, Q. Xue, Z. Wang, Z. Liu, Z. Tang, Y. Wang, F. Kang, B. Li, C. Zhi, An extremely safe and wearable solid-state zinc ion battery based on a hierarchical structured polymer electrolyte. *Energy Environ. Sci.* **11**, 941–951 (2018).
13. D. Wang, C. Han, F. Mo, Q. Yang, Y. Zhao, Q. Li, G. Liang, B. Dong, C. Zhi, Energy density issues of flexible energy storage devices. *Energy Storage Mater.* **28**, 264–292 (2020).
14. Y. Liang, H. Dong, D. Aurbach, Y. Yao, Current status and future directions of multivalent metal-ion batteries. *Nat. Energy* **5**, 646–656 (2020).
15. Lithium-ion batteries need to be greener and more ethical. *Nature* **595**, 7 (2021).
16. J. Song, K. Xu, N. Liu, D. Reed, X. Li, Crossroads in the renaissance of rechargeable aqueous zinc batteries. *Mater. Today* **45**, 191–212 (2021).
17. Y. Li, J. Fu, C. Zhong, T. Wu, Z. Chen, W. Hu, K. Amine, J. Lu, Recent advances in flexible zinc-based rechargeable batteries. *Adv. Energy Mater.* **9**, 1802605 (2019).
18. L. E. Blanc, D. Kundu, L. F. Nazar, Scientific challenges for the implementation of Zn-ion batteries. *Joule* **4**, 771–799 (2020).
19. X. Jia, C. Liu, Z. G. Neale, J. Yang, G. Cao, Active materials for aqueous zinc ion batteries: Synthesis, crystal structure, morphology, and electrochemistry. *Chem. Rev.* **120**, 7795–7866 (2020).
20. C. Liu, X. Xie, B. Lu, J. Zhou, S. Liang, Electrolyte strategies toward better zinc-ion batteries. *ACS Energy Lett.* **6**, 1015–1033 (2021).
21. F. Mo, Z. Chen, G. Liang, D. Wang, Y. Zhao, H. Li, B. Dong, C. Zhi, Zwitterionic sulfobetaine hydrogel electrolyte building separated positive/negative ion migration channels for aqueous Zn-MnO_2 batteries with superior rate capabilities. *Adv. Energy Mater.* **10**, 2000035 (2020).
22. M. Yao, Z. Yuan, S. Li, T. He, R. Wang, M. Yuan, Z. Niu, Scalable assembly of flexible ultrathin all-in-one zinc-ion batteries with highly stretchable, editable, and customizable functions. *Adv. Mater.* **33**, 2008140 (2021).
23. S. Zhang, N. Yu, S. Zeng, S. Zhou, M. Chen, J. di, Q. Li, An adaptive and stable bio-electrolyte for rechargeable Zn-ion batteries. *J. Mater. Chem. A* **6**, 12237–12243 (2018).
24. L. Mao, Q. Meng, A. Ahmad, Z. Wei, Mechanical analyses and structural design requirements for flexible energy storage devices. *Adv. Energy Mater.* **7**, 1700535 (2017).
25. S. Huang, F. Wan, S. Bi, J. Zhu, Z. Niu, J. Chen, A self-healing integrated all-in-one zinc-ion battery. *Angew. Chem. Int. Ed.* **58**, 4313–4317 (2019).
26. K. Wu, J. Huang, J. Yi, X. Liu, Y. Liu, Y. Wang, J. Zhang, Y. Xia, Recent advances in polymer electrolytes for zinc ion batteries: Mechanisms, properties, and perspectives. *Adv. Energy Mater.* **10**, 1903977 (2020).
27. R. A. Soler-Crespo, L. Mao, J. Wen, H. T. Nguyen, X. Zhang, X. Wei, J. Huang, S. B. T. Nguyen, H. D. Espinosa, Atomically thin polymer layer enhances toughness of graphene oxide monolayers. *Matter* **1**, 369–388 (2019).
28. J. L. Suter, R. C. Sinclair, P. V. Coveney, Principles governing control of aggregation and dispersion of graphene and graphene oxide in polymer melts. *Adv. Mater.* **32**, 2003213 (2020).
29. D. Devaux, R. Bouchet, D. Glé, R. Denoyel, Mechanism of ion transport in PEO/LiTFSI complexes: Effect of temperature, molecular weight and end groups. *Solid State Ion.* **227**, 119–127 (2012).
30. B. Tang, L. Shan, S. Liang, J. Zhou, Issues and opportunities facing aqueous zinc-ion batteries. *Energy Environ. Sci.* **12**, 3288–3304 (2019).
31. S. Mandal, S. Kumari, M. Kumar, U. Ojha, Supplementary networking of interpenetrating polymer system (SNIPSY) strategy to develop strong & high water content ionic hydrogels for solid electrolyte applications. *Adv. Funct. Mater.* **31**, 2100251 (2021).
32. S. Wu, M. Hua, Y. Alsaid, Y. du, Y. Ma, Y. Zhao, C. Y. Lo, C. Wang, D. Wu, B. Yao, J. Strzalka, H. Zhou, X. Zhu, X. He, Poly(vinyl alcohol) hydrogels with broad-range tunable mechanical properties via the hofmeister effect. *Adv. Mater.* **33**, 2007829 (2021).
33. M. Hua, S. Wu, Y. Ma, Y. Zhao, Z. Chen, I. Frenkel, J. Strzalka, H. Zhou, X. Zhu, X. He, Strong tough hydrogels via the synergy of freeze-casting and salting out. *Nature* **590**, 594–599 (2021).
34. C. Wang, T. He, J. Cheng, Q. Guan, B. Wang, Bioinspired interface design of sewable, weavable, and washable fiber zinc batteries for wearable power textiles. *Adv. Funct. Mater.* **30**, 2004430 (2020).
35. H. Li, Z. Liu, G. Liang, Y. Huang, Y. Huang, M. Zhu, Z. Pei, Q. Xue, Z. Tang, Y. Wang, B. Li, C. Zhi, Waterproof and tailorable elastic rechargeable yarn zinc ion batteries by a cross-linked polyacrylamide electrolyte. *ACS Nano* **12**, 3140–3148 (2018).
36. T. Xiong, Z. G. Yu, H. Wu, Y. du, Q. Xie, J. Chen, Y. W. Zhang, S. J. Pennycook, W. S. V. Lee, J. Xue, Defect engineering of oxygen-deficient manganese oxide to achieve high-performing aqueous zinc ion battery. *Adv. Energy Mater.* **9**, 1803815 (2019).
37. X. Guo, J. Zhou, C. Bai, X. Li, G. Fang, S. Liang, Zn/MnO_2 battery chemistry with dissolution-deposition mechanism. *Mater. Today Energy* **16**, 100396 (2020).
38. X. Xiao, G. Chen, A. Libanori, J. Chen, Wearable triboelectric nanogenerators for therapeutics. *Trends Chem.* **3**, 279–290 (2021).
39. Y. Fang, X. Zhao, T. Tat, X. Xiao, G. Chen, J. Xu, J. Chen, All-in-one conformal epidermal patch for multimodal biosensing. *Matter* **4**, 1102–1105 (2021).
40. K. Meng, S. Zhao, Y. Zhou, Y. Wu, S. Zhang, Q. He, X. Wang, Z. Zhou, W. Fan, X. Tan, J. Yang, J. Chen, A wireless textile-based sensor system for self-powered personalized health care. *Matter* **2**, 896–907 (2020).
41. S. Shen, X. Xiao, X. Xiao, J. Chen, Wearable triboelectric nanogenerators for heart rate monitoring. *Chem. Commun.* **57**, 5871–5879 (2021).
42. S. Shen, X. Xiao, X. Xiao, J. Chen, Triboelectric nanogenerators for self-powered breath monitoring. *ACS Appl. Energy Mater.*, (2021); https://doi.org/10.1021/acsaem.1c02465.
43. S. Zhang, M. Bick, X. Xiao, G. Chen, A. Nashalian, J. Chen, Leveraging triboelectric nanogenerators for bioengineering. *Matter* **4**, 845–887 (2021).
44. L. Jin, X. Xiao, W. Deng, A. Nashalian, D. He, V. Raveendran, C. Yan, H. Su, X. Chu, T. Yang, W. Li, W. Yang, J. Chen, Manipulating relative permittivity for high-performance wearable triboelectric nanogenerators. *Nano Lett.* **20**, 6404–6411 (2020).
45. H. A. Almohamad, S. Z. Selim, An algorithm for computing the distance between two circular disks. *Appl. Math. Model.* **27**, 115–124 (2003).
46. P. J. Flory, *Principles of Polymer Chemistry* (Cornell Univ. Press, 1953).

Acknowledgments: J.C. acknowledges the Henry Samueli School of Engineering and Applied Science and the Department of Bioengineering at the University of California, Los Angeles for the start-up support. We acknowledge Shenzhen Huasuan Technology Co. Ltd. for providing the simulation platform, X. Li and H. Zhang for providing stellar schematic diagram, and N. Zhang and J. Sima from Caltech for their stimulating insightful discussions. **Funding:** Start-up support from the University of California, Los Angeles; Discovery Early Career Researcher Award (DECRA, no. DE180101478) of the Australian Research Council and Discovery Project (DP210102215); National Key R&D Program of China (grant no. 2018YFA0306900); National Natural Science Foundation of China (no. 51872012); and Tsinghua-Foshan Innovation Special Fund (TFISF, 2020THFS0109). **Author contributions:** X.X. (first author), Y.G., W.L., and J.C. conceived the idea, designed the experiment, and guided the project. X.X., X.X., and Z.W. fabricated the batteries, performed characterization, and tested the TBAN. X.X. (first author), Z.L., C.L., and M.H. performed the simulation and calculation. X.X., X.X., and J.C. analyzed the experimental data, drew the figures, and prepared the manuscript. J.C. submitted the manuscript and was the lead contact. All authors reviewed and commented on the manuscript. **Competing interests:** The authors declare that they have no competing interests. **Data and materials availability:** All data needed to evaluate the conclusions in the paper are present in the paper and/or the Supplementary Materials. The original data for free access in general-purpose repository Dryad: https://datadryad.org/stash/share/CwCsj9o0lgCnkPIAWaXvePf2i-dUwYQxs-sZp9oo5aI.

Submitted 13 July 2021
Accepted 15 October 2021
Published 1 December 2021
10.1126/sciadv.abl3742